Applied Physics Letters

Direct measurement of anisotropic conductivity in a nanolaminated $(Mn_{0.5}Cr_{0.5})_2GaC$ thin film

Cite as: Appl. Phys. Lett. **115**, 094101 (2019); https://doi.org/10.1063/1.5115347
Submitted: 17 June 2019 . Accepted: 11 August 2019 . Published Online: 28 August 2019

Tim Flatten, Frank Matthes, Andrejs Petruhins, Ruslan Salikhov, Ulf Wiedwald, Michael Farle, Johanna Rosen, Daniel E. Bürgler, and Claus M. Schneider

Applied Physics Letters ARTICLE scitation.org/journal/apl

Direct measurement of anisotropic conductivity in a nanolaminated $(Mn_{0.5}Cr_{0.5})_2GaC$ thin film

Cite as: Appl. Phys. Lett. **115**, 094101 (2019); doi: 10.1063/1.5115347
Submitted: 17 June 2019 · Accepted: 11 August 2019 ·
Published Online: 28 August 2019

Tim Flatten,[1,2,a)] Frank Matthes,[1,2] Andrejs Petruhins,[3] Ruslan Salikhov,[4] Ulf Wiedwald,[4] Michael Farle,[4] Johanna Rosen,[3] Daniel E. Bürgler,[1,2] and Claus M. Schneider[1,2,4]

AFFILIATIONS

[1]Peter Grünberg Institut (PGI-6), Forschungszentrum Jülich, D-52425 Jülich, Germany
[2]Jülich-Aachen Research Alliance (JARA-FIT), D-52425 Jülich, Germany
[3]Thin Film Physics Division, Department of Physics, Chemistry and Biology (IFM), Linköping University, SE-58183 Linköping, Sweden
[4]Faculty of Physics and Center for Nanointegration (CENIDE), University of Duisburg-Essen, 47057 D-Duisburg, Germany

[a)]**Electronic mail:** t.flatten@fz-juelich.de

ABSTRACT

The direct and parameter-free measurement of anisotropic electrical resistivity of a magnetic $M_{n+1}AX_n$ (MAX) phase film is presented. A multitip scanning tunneling microscope is used to carry out 4-probe transport measurements with variable probe spacing s. The observation of the crossover from the 3D regime for small s to the 2D regime for large s enables the determination of both in-plane and perpendicular-to-plane resistivities ρ_{ab} and ρ_c. A $(Cr_{0.5}Mn_{0.5})_2GaC$ MAX phase film shows a large anisotropy ratio $\rho_c/\rho_{ab} = 525\pm49$. This is a consequence of the complex bonding scheme of MAX phases with covalent M–X and metallic M–M bonds in the MX planes and predominately covalent, but weaker bonds between the MX and A planes.

In recent years, layered materials such as graphite, hexagonal boron nitride, and transition metal dichalcogenides have attracted great interest due to their intriguing fundamental properties and their high potential in a variety of applications since their highly anisotropic crystallographic structure, which comprises covalently coordinated two-dimensional atomic layers that are stacked and van der Waals-bonded in the third dimension, carries over to anisotropic electronic, optical, and mechanical properties of the bulk material.[1,2] The ternary carbides and nitrides with the general formula $M_{n+1}AX_n$ (MAX) with $n = 1, 2, 3$ (M is an early transition metal, A is an A-group element mostly of the main groups 13–16, and X is C or N) represent a further material class with nanolaminated and anisotropic atomic structures, but with predominantly covalent bonds both within the two-dimensional building blocks formed by M-X-M planes and between them. As a consequence, MAX phases combine metallic and ceramic properties in a unique manner.[3] MAX phases are electrically and thermally conductive, thermally stable, elastically stiff, light-weight, and readily machinable.[4] Great potential of MAX phases in applications ranging from electrical contacts, magnetic sensors, spintronics devices to coating materials in aerospace technology[5–7] has triggered the development of an environmentally friendly, sustainable, and cheap MAX phase synthesis scheme that can be scaled up to industrial scale.[8]

Electrical conductivity is a key property of any material and often of decisive relevance for its application. Hence, in the last four decades, research on the measurement of anisotropic electrical transport has increased.[9,10] The transport properties of a solid are characterized by the second-rank resistivity tensor $\boldsymbol{\rho}$ comprising a symmetry-dependent number of independent components that can be determined from resistance measurements along different directions of the sample. Several modified versions of the van der Pauw technique can be used for the measurement of anisotropic resistivity components in the surface plane of a sample.[10–14] However, this straight-forward determination of the in-plane resistivities ρ_a and ρ_b becomes quite challenging if the out-of-plane resistivity ρ_c has to be taken into account as well. Then, the sample must be cut to get access to another crystalline surface orientation,[10] which is inherently difficult for samples synthesized in thin-film form. This particularly applies to MAX phases, which due to the crystalline asymmetry predominantly grow in (0001) orientation (i.e., in c-direction), thus preventing the determination of $\rho_{a,b}$ and ρ_c by measuring two suitably oriented thin-film samples. There are some alternative strategies for measuring ρ_c that we briefly discuss in the following in the context of experimental data for MAX phases. A direct measurement of ρ_c[15] requires sufficiently large single crystals that are difficult to grow and patterning efforts to achieve a specific device structure,[16] which allows us to extract ρ_c using geometric correction factors. Individual grains of a polycrystalline sample can be addressed with transmission electron microscopy measuring the dielectric response in different crystalline orientations by electron energy loss spectroscopy. Subsequent semiclassical Drude–Lorentz modeling then provides an estimate of the resistivity anisotropy.[17,18] The comparison of the in-plane resistivity measurement of a (0001)-oriented thin film (yielding $\rho_{a,b}$) with the resistivity of a polycrystalline bulk sample (which depends on both $\rho_{a,b}$ and ρ_c) allows deducing the resistivity anisotropy in an effective medium approach.[19,20] However, the large parameter space of effective medium models and different defect and impurity densities result in large uncertainties.

Here, we report a parameter-free experimental procedure to accurately measure both ρ_{ab} and ρ_c from a single (0001)-oriented MAX phase thin film. The method is based on 4-probe measurements with variable probe spacings realized by a 4-probe scanning tunneling microscope (STM) featuring for all four probes individual lateral positioning and a well-defined vertical approach to the contact regime. Regarding the samples, this method is based on only one single oriented thin-film sample and does neither require a specific device structure nor a comparison of samples with different microstructures or modeling of transport or effective medium properties. A (0001)-oriented $(Cr_{0.5}Mn_{0.5})_2GaC$ MAX phase film yields $\rho_{ab} = (1.14 \pm 0.04)\ \mu\Omega$ m and a large resistivity anisotropy ratio $\rho_c/\rho_{ab} = 525 \pm 49$.

The two-dimensional building blocks of $M_{n+1}AX_n$ phases are evident in the crystal structure for $n = 1$ shown in Fig. 1(a). M_2X layers formed by face-sharing M_6X octahedrons and planar A layers are stacked alternately along the *c*-axis. As a consequence, MAX phases exhibit chemical bonding anisotropy.[6] All bonds are predominantly of covalent character with different degrees of admixed metallicity or ionicity.[6] The mixed bonding character gives rise to the combined metallic and ceramic properties of MAX phases. Strong hybridization between the *d*-orbitals of the M elements and the 2*p*-orbitals of the X elements leads to M-X-M chains with strong covalent pd_σ and pd_π bonds as schematically shown in Figs. 1(b) and 1(c), respectively. The primarily covalent M-A bonds between the M_2X and A planes sketched in Fig. 1(e) are typically weaker than the M-X bonds. The *d*-orbitals of the M elements also form metal-metal dd_σ bonds with adjacent M atoms [Fig. 1(d)]. The energy of these states, which are spatially confined in the M_2X layers, is in vicinity of the Fermi level E_F. These states dominate the overall density of states at E_F and accordingly also the electric conductivity, which is thereby much higher in the *ab* plane compared to the *c*-direction.[6] This is corroborated by density-functional theory (DFT) calculations of band structures of various MAX phases. Most MAX phases do not have bands that cross the Fermi surface along the *c*-axis.[5] Therefore, the anisotropy in the electronic structure is theoretically predicted to lead to anisotropic electronic transport. The anisotropy of the transport may be further enhanced by electron-phonon interaction.[20] Typically, the resistivity (inverse conductivity) in the *ab*-plane $\rho_{ab} \equiv \rho_a = \rho_b$ is significantly lower than the resistivity along the *c*-axis ρ_c,[5,6,15,21] where ρ_{ab} and ρ_c are the two independent components of the diagonal second-ranked resistivity tensor with respect to the hexagonal structure of the MAX phases.

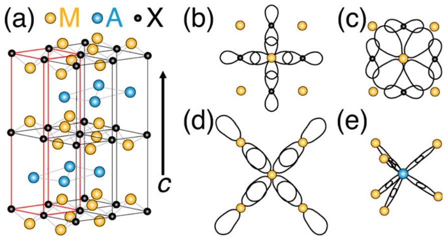

FIG. 1. (a) Layered crystal structure of M_2AX phases. The red lines indicate the unit cell. Bonds in the M_2X layer: (b) Covalent M–X pd_σ bonds, (c) covalent M–X pd_π bonds, and (d) mixed covalent-metallic M–M dd_σ bonds. (e) Covalent M–A pd_σ bonds between M_2X and A layers. (b)–(e) are reprinted with permission from M. Magnuson and M. Mattesini, Thin Solid Films **621**, 108–130 (2017). Copyright 2017, Elsevier.

The resistance *R* measured in a 4-probe configuration depends not only on the intrinsic resistivity tensor $\boldsymbol{\rho}$ of the sample and on the configuration of the contact probes but also on the shape and dimension of the sample. We exploit the interplay between these dependencies to extract the anisotropy between ρ_{ab} and ρ_c. Parasitic resistances of the probe-sample contacts and the leads are negligible in the 4-probe configuration,[9] as separate pairs of probes are used for injecting the current *I* and detecting the voltage drop *V* [Figs. 2(a) and 2(b)].

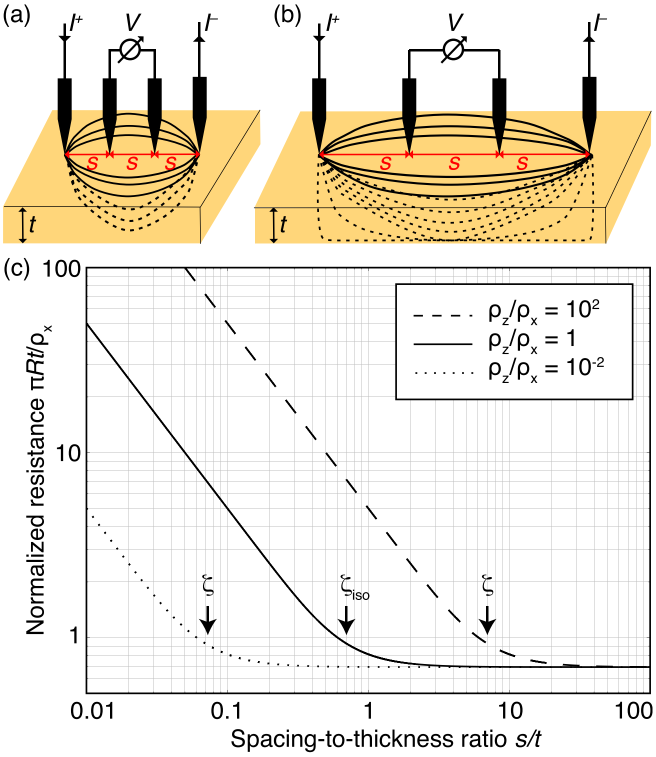

FIG. 2. Crossover between 3D and 2D electron transport regimes. Sketches of 4-probe transport measurements in a film with thickness *t* and equidistant probe spacing *s* for (a) $s \ll t$ (3D case) and (b) $s \gg t$ (2D case) according to Ref. 9. Dashed lines indicate the current distribution, which is unperturbed spherical in the 3D case, but compressed at the sample bottom in the 2D case. (c) Transient behavior of the normalized resistance as a function of the normalized probe spacing *s*/*t* according to Eq. (6) for isotropic (solid line) and different anisotropic resistivities (dotted and dashed) as indicated.

Expressions for the measured resistance $R = V/I$ have previously been derived for isotropic resistivity $\rho_{\mathrm{iso}} \equiv \rho_{\mathrm{ab}} = \rho_{\mathrm{c}}$ in two limiting cases, namely, for an infinitely thick, three-dimensional (3D) sample and a thin, two-dimensional (2D) sample[22]

$$R^{3\mathrm{D}} = \frac{\rho_{\mathrm{iso}}}{2\pi s} \quad \text{for} \quad t \gg s, \tag{1}$$

$$R^{2\mathrm{D}} = \frac{\rho_{\mathrm{iso}}}{\pi t}\ \ln(2) \quad \text{for} \quad t \ll s, \tag{2}$$

where s is the equidistant probe spacing and t the sample thickness. In the 3D case, the current spreads spherically from the injection points, and $R^{3\mathrm{D}} \propto s^{-1}$. For the 2D case, the current spreading is cylindrical, because the current distribution is compressed at the sample bottom due to the finite film thickness, and R is independent of s, but $R^{2\mathrm{D}} \propto t^{-1}$. These s dependencies are against common experience, which is based on 1D measurements of long wires with $R^{1\mathrm{D}} \propto s$. In the 2D and 3D cases, the increase in resistance along each current path is compensated (2D) or overcompensated (3D) by the increasing number of current paths.[9] In Figs. 2(a) and 2(b), the crossover from the 3D to the 2D case is accomplished by varying s instead of t from $s \ll t$ to $s \gg t$, which is key for the here presented measurement procedure to determine the resistivity anisotropy of a thin film with homogeneous resistivity. The different s dependencies for the 3D and 2D cases have previously been used to separate surface and bulk contributions to the conductivity at semiconductor and ternary transition metal oxide surfaces.[23,24] Their spatially inhomogeneous conductivity $\sigma(z)$ is described in the N-layer model[25] by layers with different, but isotropic resistivity values.

For a given geometry of current injection, the potential is given by the Laplace equation. Albers and Berkowitz presented an approximate solution for the crossover from the 3D to the 2D region for the case of isotropic resistivity $\rho_{\mathrm{iso}} \equiv \rho_{\mathrm{x}} = \rho_{\mathrm{y}} = \rho_{\mathrm{z}}$,[26]

$$R = \frac{\rho_{\mathrm{iso}}}{\pi t} \cdot \ln\left(\frac{\sinh(t/s)}{\sinh(t/2s)}\right). \tag{3}$$

In Fig. 2(c), we show this transient behavior by plotting dimensionless normalized resistance $\pi R t/\rho_{\mathrm{iso}}$ as a function of normalized probe spacing s/t (solid line). The crossover from the 3D behavior in the left part of the curve with $R \propto s^{-1}$ to the 2D case in the right part, for which R does not dependent on s, occurs at

$$\zeta_{\mathrm{iso}} = \frac{s}{t} = \frac{1}{2\ \ln(2)}, \tag{4}$$

where $R^{3\mathrm{D}} = R^{2\mathrm{D}}$ [see Eqs. (1) and (2)]. This result is only valid for isotropic resistivity as indicated by the index "iso." For s/t ratios exceeding this value, the finite thickness of the sample affects and compresses the spatial current distribution as sketched in Figs. 2(a) and 2(b).

The accuracy of the Albers-Berkowitz approximation has been investigated experimentally[27] and theoretically,[28] and it was found that the approximate resistance values deviate by less than 10% near the crossover point ζ_{iso} and much less elsewhere. Note that the approximation does not affect the accuracy of the determination of crossover point and the anisotropy ratio derived therefrom [see below and Eq. (7)], since these quantities are obtained from the intersection of the (exact) curves for the 2D and 3D regimes [Eqs. (1) and (2)]. In supplementary material 1, we generalize the crossover function in Eq. (3) for arbitrary probe positions and apply it to the square configuration and to in-line configurations when only two of the four probe positions are varied to observe the 3D-2D crossover.

If we now consider an anisotropic resistivity with enhanced (reduced) resistivity normal to the sample surface, then the current distribution will be deformed such that the current flow is closer to (farther from) the sample surface. Accordingly, the onset of the perturbation due to the finite thickness of the sample and, thus, the 3D-2D crossover will be shifted to smaller (larger) sample thickness. For the formal description of this effect, we restrict ourselves to crystallographic symmetries (cubic, tetragonal, hexagonal, trigonal, and orthorhombic), for which the resistivity tensor is diagonal and comprises three resistivity components ρ_{x}, ρ_{y}, and ρ_{z}. For the treatment of an anisotropic sample, van der Pauw[29] suggested a transformation of the coordinates of an anisotropic cube with edge length l onto an isotropic parallelepiped of resistivity ρ and dimensions l_i',

$$l_i' = \sqrt{\frac{\rho_i}{\rho}}\, l \quad \text{with} \quad i = x, y, z, \tag{5}$$

where $\rho = \sqrt[3]{\rho_{\mathrm{x}} \cdot \rho_{\mathrm{y}} \cdot \rho_{\mathrm{z}}}$. This transformation does not affect the resistance R as it preserves voltage and current.[9] Without loss of generality, we define the coordinate system so that the sample surface lies in the xy plane and the probes are aligned along the x-axis. Applying the above transformation to Eqs. (1)–(4) yields general expressions for the 3D-2D transient behavior for anisotropic samples

$$R = \frac{\sqrt{\rho_{\mathrm{x}}\rho_{\mathrm{y}}}}{\pi t} \cdot \ln\left(\frac{\sinh\left(\sqrt{\frac{\rho_{\mathrm{z}}}{\rho_{\mathrm{x}}}} \cdot t/s\right)}{\sinh\left(\sqrt{\frac{\rho_{\mathrm{z}}}{\rho_{\mathrm{x}}}} \cdot t/2s\right)}\right), \tag{6}$$

$$\zeta = \frac{s}{t} = \frac{\sqrt{\rho_{\mathrm{z}}/\rho_{\mathrm{x}}}}{2\ \ln(2)}. \tag{7}$$

Equation (6) is plotted in Fig. 2(c) for different anisotropy ratios of the perpendicular-to-plane and in-plane resistivities $\rho_{\mathrm{z}}/\rho_{\mathrm{x}} = 10^2$ (dashed), 1 (solid), and 10^{-2} (dotted), for clarity under the assumption $\rho_{\mathrm{x}} = \rho_{\mathrm{y}}$. Obviously, the crossover between the 2D and 3D cases depends on the anisotropy ratio, as explained above phenomenologically. For fixed sample thickness t, the crossover occurs for $\rho_{\mathrm{x}} < (>) \rho_{\mathrm{z}}$ at larger (smaller) probe spacing s. Equations (6) and (7) quantify the anisotropy-dependent shift of the 3D-2D crossover point ζ and reveal a parameter-free method to determine the anisotropy ratio $\rho_{\mathrm{z}}/\rho_{\mathrm{x}}$ from the measurement of the 3D-2D crossover.

Experimentally, we apply this scheme to the MAX phase $(\mathrm{Cr}_{0.5}\mathrm{Mn}_{0.5})_2\mathrm{GaC}$[30] to directly measure the resistivity anisotropy. $(\mathrm{Cr}_{0.5}\mathrm{Mn}_{0.5})_2\mathrm{GaC}$ has attracted interest due to its peculiar spin structure and resulting magnetic properties that both originate from the nanolaminated crystal structure.[30,31] Our thin-film sample with thickness $t = 155\,\mathrm{nm}$ was grown at Linköping University by magnetron sputter epitaxy on a MgO(111) substrate.[30] X-ray diffraction and transmission electron microscopy have proven the MAX phase structure on MgO(111) with $[11\bar{2}0]_{\mathrm{MAX}} || [10\bar{1}]_{\mathrm{MgO}}$ in the surface plane and $[0001]_{\mathrm{MAX}} || [111]_{\mathrm{MgO}}$ out of the plane, i.e., the a and b axes lying in the thin-film plane and the c axis along the surface normal. Hence, we can identify $\rho_{\mathrm{ab}} \equiv \rho_{\mathrm{a}} = \rho_{\mathrm{x}} = \rho_{\mathrm{b}} = \rho_{\mathrm{y}}$ as the in-plane resistivity and

$\rho_c \equiv \rho_z$ as the out-of-plane resistivity. The 4-probe transport measurements are performed at room temperature with a 4-probe STM (LT Nanoprobe from Scienta Omicron), which is operated in ultrahigh vacuum (UHV, base pressure $<5 \times 10^{-10}$ mbar) and features a top-mounted scanning electron microscope (SEM) for monitoring the probe positioning. Tungsten probes are wet-chemically etched and flash-annealed in the UHV system to remove oxides. Before the transport measurements each probe is inspected in the SEM to ensure a probe diameter of less than 200 nm. After transfer into UHV, the sample was annealed for 1 h at 150 °C to desorb physisorbed contaminants from the chemically inert surface. For each resistance measurement, the four STM probes are first positioned under SEM control in an in-line configuration with the desired equidistant probe spacing s [Fig. 3(a)]. Experimental challenges limiting the smallest probe spacing for our setup to 1 μm are discussed in the supplementary material 2. Each probe is then approached into the tunneling regime (typically 1 nA tunneling current at 1 V bias voltage) using the approach procedure of the STM controller. Finally, the probes are individually moved (using the z-axes of the STM piezo scanners) by about 1 nm toward the sample to establish Ohmic contacts. This gentle procedure ensures that the contact diameters do not exceed 200 nm,[32] and therefore, they have no significant influence on the measurement (see supplementary material 3). For the resistance measurements, the probes are disconnected from the STM controller and connected to a current source and a voltmeter. The current I is injected from a current source (Keithley 2636A) through the outer probes (I^+ and I^-), and the voltage drop V between the inner probes (V^+ and V^-) is measured by a digital multimeter (Agilent 3458A). The current is swept from -1.0 to $+1.0$ mA to record a V-I curve [red dots in Fig. 3(b)], from which we obtain the resistance R by fitting the linear function $V(I) = R \cdot I + V_0$ [blue curve in Fig. 3(b)]. V_0 is always of the order of 50 μV and thus much smaller than the voltage drop. The error bar of the resistance values is within 0.1%.

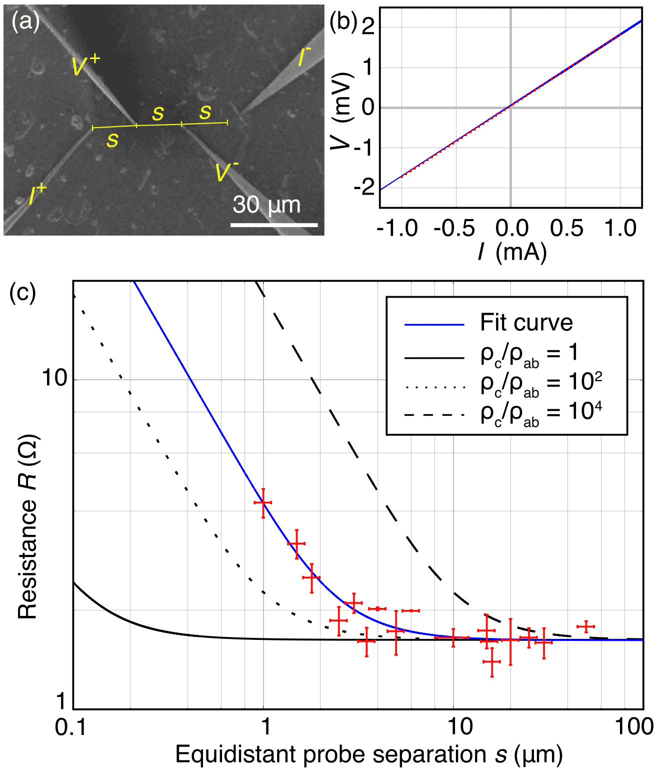

FIG. 3. 4-probe transport measurements of a 155 nm thick $(Cr_{0.5}Mn_{0.5})_2GaC$ thin film. (a) SEM image of an in-line configuration with equidistant probe spacing s. (b) V-I curve for $s = 15\ \mu$m. Red dots are measured values (including error bars), and the blue line is a linear fit yielding $R = (1.7738 \pm 0.0005)\ \Omega$ and $V_0 = (51.0 \pm 0.2)\ \mu$V. (c) Measured resistances R (red) vs equidistant probe spacing s. The blue curve is a fit of Eq. (6) to the data yielding $\rho_c/\rho_{ab} = (525 \pm 49)$. Black curves show for comparison the isotropic behavior (solid line) and anisotropic cases for anisotropy ratios 10^2 (dotted) and 10^4 (dashed).

Figure 3(c) shows a compilation of 38 resistance measurements (red symbols) for a set of probe spacings ranging from $s = 1$ to 50 μm that were performed with numerous probes and at several spots of the sample surface as well as in different in-plane directions. For each probe spacing s, we plot the mean R with an error bar both obtained by averaging several measurements, each consisting of positioning and approach of the probes followed by recording and fitting a V-I curve. The thus determined errors of R are typically about 10% that can be traced back to the uncertainty of the probe positioning, in particular, along the line connecting the probes, of 5%–10% as discussed in the supplementary material 3. For s values, where only one R measurement could be obtained, the same relative error is assumed. Obviously, R is constant for large s and increases for $s < 5\ \mu$m. This behavior can be fitted in a parameter-free manner with the transient behavior described by Eq. (6) as shown by the solid blue line. The least-squares fitting simultaneously yields both $\rho_{ab} = (1.14 \pm 0.04)\ \mu\Omega$ m and $\rho_c = (599 \pm 52)\ \mu\Omega$ m, leading to the anisotropy ratio $\frac{\rho_c}{\rho_{ab}} = 525 \pm 49$ and the 3D-2D crossover point $\zeta t = (2.6 \pm 0.1)\ \mu$m. The low in-plane resistivity ρ_{ab} confirms theoretical predictions[5,6,15,21] and is in the range of experimental values reported for various MAX phases.[6,15,20] In particular, the value compares well with the resistivity $\rho_{poly} = 2.2\ \mu\Omega$ m reported by Lin *et al.*[33] for sintered polycrystalline $(Cr_{0.5}Mn_{0.5})_2GaC$ pellet samples, for which the impact of ρ_c is largely suppressed because the current paths can pass primarily in the *ab*-planes of the crystallites due to current percolation. While numerous theoretical reports predict that in MAX phases $\rho_c \gg \rho_{ab}$,[5,6,15] there are only very few experimental data on the anisotropy ratio and no previous measurement for the $(Cr_{0.5}Mn_{0.5})_2GaC$ MAX phase. Our result $\frac{\rho_c}{\rho_{ab}} = 525 \pm 49$ clearly deviates from the isotropic case [black solid line in Fig. 3(c)] found for the Ti_2GeC MAX phase[19] and also exceeds the ratio of 14–18 reported for the Ti_2AlC MAX phase.[20] However, it is of the same order of magnitude as reported for Cr_2AlC (300–475 at 300 K) and V_2AlC (3000–9000 between 300 and 4 K) MAX phases.[15] For comparison, the dotted and dashed lines in Fig. 3(c) indicate the transient behavior for $\rho_{ab} = 1.14\ \mu\Omega$ m and anisotropy ratios 10^2 and 10^4, respectively.

In conclusion, we have measured the in-plane and perpendicular-to-plane resistivities of a nanolaminated MAX phase thin film using a specifically developed parameter-free experimental procedure, which is based on 4-probe measurements with variable probe spacings performed with a 4-probe STM. This method relies on a single oriented thin-film sample and does neither require a specific device structure nor a comparison of samples with different microstructures or modeling of transport or effective medium properties. In particular, it can be applied to materials that are not available as micrometer-thick crystals or are unstable unless stabilized in thin film form. Concerning MAX phase films, the method enables the characterization of anisotropic electrical transport with unprecedented accuracy, reliability, and ease of sample fabrication, allowing for systematic studies of the impact of the chemical composition on the resistivity tensor in order to achieve a deeper understanding of the electronic structure of MAX phases. The measured sizable resistivity anisotropy of a $(Cr_{0.5}Mn_{0.5})_2GaC$ MAX phase thin film $\rho_c/\rho_{ab} = 525 \pm 49$ reflects the complex bonding scheme of MAX phases with predominately covalent bonds in the basal planes as well as between the MX and A planes, but mixed with different degrees of metallicity and ionicity, resulting in the unique combination of metallic and ceramic properties of MAX phases. Our data provide clear evidence for a sizable resistance anisotropy in a magnetic MAX phase, thus opening an avenue for investigating the so far unexplored interplay between electronic structure near the Fermi surface and the magnetic order that may add novel spintronic functionality to the versatile class of magnetic MAX phases.

See the supplementary material for (i) a generalized expression for 4-point transport measurements with arbitrary probe positioning, (ii) details about the control of small lateral probe spacings, and (iii) a discussion of sources for the error of four-probe resistance measurements.

J.R. acknowledges support from the Knut and Alice Wallenberg (KAW) Foundation for a Fellowship Grant as well as from the Swedish Research Council through Project No. 642-2013-8020.

REFERENCES

[1] K. S. Novoselov, V. I. Fal'ko, L. Colombo, P. R. Gellert, M. G. Schwab, and K. Kim, Nature **490**, 192 (2012).
[2] K. S. Novoselov, A. Mishchenko, A. Carvalho, and A. H. Castro Neto, Science **353**, aac9439 (2016).
[3] M. W. Barsoum, Prog. Solid State Chem. **28**, 201 (2000).
[4] M. W. Barsoum, *MAX Phases: Properties of Machinable Ternary Carbides and Nitrides* (Wiley-VCH, 2013).
[5] P. Eklund, M. Beckers, U. Jansson, H. Högberg, and L. Hultman, Thin Solid Films **518**, 1851 (2010).
[6] M. Magnuson and M. Mattesini, Thin Solid Films **621**, 108 (2017).
[7] I. P. Novoselova, A. Petruhins, U. Wiedwald, D. Weller, J. Rosen, M. Farle, and R. Salikhov, Mater. Res. Lett. **7**, 159 (2019).
[8] A. Dash, R. Vaßen, O. Guillon, and J. Gonzalez-Julian, Nat. Mater. **18**, 465 (2019).
[9] I. Miccoli, F. Edler, H. Pfnür, and C. Tegenkamp, J. Phys.: Condens. Matter **27**, 223201 (2015).
[10] C. A. M. dos Santos, A. de Campos, M. S. da Luz, B. D. White, J. J. Neumeier, B. S. de Lima, and C. Y. Shigue, J. Appl. Phys. **110**, 083703 (2011).
[11] J. D. Wasscher, Philips Res. Rep. **16**, 301 (1961).
[12] H. C. Montgomery, J. Appl. Phys. **42**, 2971 (1971).
[13] K. A. Borup, K. F. F. Fischer, D. R. Brown, G. J. Snyder, and B. B. Iversen, Phys. Rev. B **92**, 045210 (2015).
[14] P. Walmsley and I. R. Fisher, Rev. Sci. Instrum. **88**, 043901 (2017).
[15] T. Ouisse, L. Shi, B. A. Piot, B. Hackens, V. Mauchamp, and D. Chaussende, Phys. Rev. B **92**, 045133 (2015).
[16] M. Charalambous, J. Chaussy, and P. Lejay, Phys. Rev. B **45**, 5091 (1992).
[17] N. Haddad, E. Garcia-Caurel, L. Hultman, M. W. Barsoum, and G. Hug, J. Appl. Phys. **104**, 023531 (2008).
[18] V. Mauchamp, G. Hug, M. Bugnet, T. Cabioc'h, and M. Jaouen, Phys. Rev. B **81**, 035109 (2010).
[19] T. H. Scabarozi, P. Eklund, J. Emmerlich, H. Högberg, T. Meehan, P. Finkel, M. Barsoum, J. Hettinger, L. Hultman, and S. Lofland, Solid State Commun. **146**, 498 (2008).
[20] V. Mauchamp, W. Yu, L. Gence, L. Piraux, T. Cabioc'h, V. Gauthier, P. Eklund, and S. Dubois, Phys. Rev. B **87**, 235105 (2013).
[21] A. Thore, M. Dahlqvist, B. Alling, and J. Rosén, J. Appl. Phys. **116**, 103511 (2014).
[22] L. Valdes, Proc. IRE **42**, 420 (1954).
[23] I. Shiraki, F. Tanabe, R. Hobara, T. Nagao, and S. Hasegawa, Surf. Sci. **493**, 633 (2001).
[24] A. Leis, C. Rodenbücher, K. Szot, V. Cherepanov, F. S. Tautz, and B. Voigtländer, Sci. Rep. **9**, 2476 (2019).
[25] S. Just, M. Blab, S. Korte, V. Cherepanov, H. Soltner, and B. Voigtländer, Phys. Rev. Lett. **115**, 066801 (2015).
[26] J. Albers and H. L. Berkowitz, J. Electrochem. Soc. **132**, 2453 (1985).
[27] J. J. Kopanski, J. Albers, G. P. Carver, and J. R. Ehrstein, J. Electrochem. Soc. **137**, 3935 (1990).
[28] R. A. Weller, Rev. Sci. Instrum. **72**, 3580 (2001).
[29] L. J. van der Pauw, Philips Res. Rep. **16**, 187 (1961).
[30] A. Petruhins, A. S. Ingason, J. Lu, F. Magnus, S. Olafsson, and J. Rosen, J. Mater. Sci. **50**, 4495 (2015).
[31] R. Salikhov, A. S. Semisalova, A. Petruhins, A. S. Ingason, J. Rosen, U. Wiedwald, and M. Farle, Mater. Res. Lett. **3**, 156 (2015).
[32] S. Just, H. Soltner, S. Korte, V. Cherepanov, and B. Voigtländer, Phys. Rev. B **95**, 075310 (2017).
[33] S. Lin, P. Tong, B. S. Wang, Y. N. Huang, W. J. Lu, D. F. Shao, B. C. Zhao, W. H. Song, and Y. P. Sun, J. Appl. Phys. **113**, 053502 (2013).